

# PHYSICS BASED VALIDATION OF AN IMPROVED NUMERICAL TECHNIQUE FOR SOLVING THERMAL FLUID RELATED PROBLEMS

**Julio Mendez, David Dodoo-Amoo, Mookesh Dhanasar and Frederick Ferguson**  
Mechanical Engineering Department, NCAT, Greensboro, NC 27411, USA

## ABSTRACT

Computational Fluid Dynamics (CFD) solutions have played an important role in the design of modern air and space transportation. CFD is also playing a significant role in the designing of new devices, such as, hypersonic airframes and propulsion systems, scramjet and ramjets. CFD is now providing the much needed guidance to designers, since analytical solutions are not available and in many cases, experimental conditions cannot be reproduced. CFD provides useful information, such that, when used along with traditional wind tunnel data enhances the understanding of pertinent fluid phenomena. However, notwithstanding its importance over the last two decades, CFD have so far failed to provide a unique method capable of solving a wide range of fluid dynamic problems, accurately, efficiently and inexpensively. The research conducted herein seeks to enhance current CFD capability by eliminating this major drawback. A CFD survey concluded that a novel scheme called *Integro-Differential Scheme* (IDS) Ferguson et al.<sup>1</sup> may have the capability to alleviate the limitations CFD currently experiences.

The focus of this research is therefore to demonstrate that IDS has the capability to solve a wide variety of CFD problems accurately, efficiently and inexpensively. In particular, the focus of this paper is to demonstrate that the IDS methodology has the capability of accurately predicting complex flow physics under realistic conditions. To this end, this paper focuses on the accuracy with which the IDS captures the complex flow physics associated with multiple shock interactions in the midst of boundary layer separation and flow field expansion. Further, in efforts to directly highlight this capability, a set of Flow Physics Extraction Functions (FPEF) were developed and implemented. These functions use the primitive variables to detect shocks and expansion waves, separation and recirculation zones, and zones with high unsteadiness and vortices. The FPEF approach supplements the traditional way of exploring datasets using contour plots of primitive variables. The two problems of interest are: (i) the 'inviscid-viscous' interactions associated with the boundary layer at the leading edge of a hypersonic flat plate, and (ii) the interactions due to the injection of a high pressure sonic jet into supersonic cross flow. The results obtained from this study are very encouraging, as they demonstrated that the IDS has the capabilities of accurately predicting the fluid physics associated with complex fluid flows under realistic Reynolds numbers.

## INTRODUCTION

The equations that govern fluid flows are described by the conservation of mass, momentum and energy principles. These equations, when coupled, are known as the Navier-Stokes Equations (NSE). The coupled NSE form a set of nonlinear partial differential equations which lend themselves to analytical solutions only under 'highly simplified' scenarios. In general, the

mathematical behavior of the NSE is complex and unpredictable. It is not possible to categorize the NSE strictly as hyperbolic, elliptic and parabolic types, as the NSE is very sensitive to the properties of its boundary and initial conditions. The very nature of the NSE make the implementation of most numerical methods very unpredictable when they are tasked in providing the solutions.

One commonly acceptable numerical procedure for solving the NSE is the method of directly resolving all the temporal and spatial scales. This approach is known as Direct Numerical Simulations (DNS). However, the computational cost associated with the DNS approach is prohibitively expensive. In fact, for three dimensional problems, the computational cost is determined to be function the Reynolds number, that can be expressed in the order of  $N$ , such that,  $N = O(Re^{9/4})$ <sup>2</sup>. Consequently, solving fluid flow problems for realistic engineering applications will not be routinely possible in the near future using DNS. On the other hand, current experimental facilities are not always capable of simulating the solution required by aircraft designers and propulsion engineers. In efforts to extend the capability of today's CFD, this research focuses on a CFD solution method for the NSE, the so-called Integro-Differential Scheme<sup>1</sup> (IDS). The IDS is potentially accurate, efficient and inexpensive and is applicable to a wide range of fluid problems under realistic boundary conditions.

The main objective of this research is to both qualitatively and quantitatively verify the physics predicted by the IDS solution when it is applied to the NSE for high Reynolds numbers. Previous studies Ferguson et al.<sup>3, 1, 4</sup> have shown that the IDS scheme is accurate. However, these studies<sup>3, 1, 4</sup> relied on the traditional way of exploring the solution space, and did not effectively demonstrated the physics capturing capabilities of the IDS<sup>5, 6</sup>. In general, the previously established techniques that are based on the manipulation of the primitive variables cannot be relied upon to accurately detect shock and expansion waves, and other flow field phenomena. Rather, physics based methods that are designed to extract meaningful information from CFD solutions are preferred. An important part of this research effort was dedicated to the creation and implementation of flow physics extractions functions (FPEF). This paper briefly describes these FPEF and discussed their findings in relations to fluid flow problems.

## THE NAVIER-STOKES EQUATIONS

In this research project, the NSE are of paramount importance and they are listed as follows:

$$\frac{\partial \rho}{\partial t} + \frac{\partial(\rho u_k)}{\partial x_k} = 0 \quad (1)$$

$$\frac{\partial \rho u_i}{\partial t} + \frac{\partial(\rho u_k u_k + p \delta_{ik} - \tau_{ik})}{\partial x_k} = 0 \quad (2)$$

$$\frac{\partial(\rho e)}{\partial t} + \frac{\partial(\rho(e + RT)u_k - \tau_{ik}u_i + q_k)}{\partial x_k} = 0 \quad (3)$$

respectively. In Equations (1 - 3) the symbols;  $\rho$ ,  $u_k$ ,  $t$ , represent the density, the velocity components of an elementary control fluid element, and time, respectively. In addition, the

symbols,  $e$ ,  $p$ ,  $\tau_{ik}$  and  $q_k$ , in equations (1 - 3) represent the internal energy, the pressure, the stress tensor and the heat flux associated with an elementary control volume. Again, in this research, internal energy, pressure, stress tensor and heat flux are defined by:

$$e = C_v T + \frac{1}{2} u_k u_k \quad (4)$$

$$P = \rho R T \quad (5)$$

$$\tau_{ik} = \mu \left( \frac{\partial u_i}{\partial x_k} + \frac{\partial u_k}{\partial x_i} \right) - \frac{2}{3} \mu \delta_{ik} \frac{\partial u_j}{\partial x_j} \quad (6)$$

$$q_k = -k \frac{\partial T}{\partial x_k} \quad (7)$$

respectively. In equation (5),  $R$  is the gas constant. The symbols,  $\mu$ , and  $k$ , represent the viscous and thermal properties of the fluid of interest. For air, the viscosity of the fluid is evaluated through the use of Sutherland's law<sup>9</sup>,

$$\mu = \mu_\infty \left( \frac{T}{T_\infty} \right)^{3/2} \frac{T_\infty + 110}{T + 110} \quad (8)$$

and the thermal conductivity expression,

$$k = f(T) \quad (9)$$

is provided. In the case of 3D aerodynamic analysis, the Navier-Stokes equations (1)–(9) defined above can be treated as a closed system of five equations relative to five unknowns. These unknowns are the following five primitive flow field variables:  $[\rho, u_k, T]$ ,  $k=1, 2, 3$ . It is of interest to note that equations (1 - 9) generates a unique solution set, only when an appropriate set of initial and boundary conditions are provided. The primitive variables associated with equations (1-9) are evaluated using the IDS procedure, which was described in Ferguson et al.<sup>1</sup>, and as such, the details are not repeated herein.

## FLOW PHYSICS EXTRACTION FUNCTIONS (FPEF)

When solving a given fluid dynamic problem, preferably one with complex interactions, it becomes important to identify the size, location and strength of the relevant flow phenomena occurring within the field. Of greater importance is the fact that unbiased measures are needed to qualify these phenomena along with their relative strengths and sizes in the regions of interest. In an effort to identify the associated flow physics predicted by the IDS procedure specialized FPEF were created as part of this research effort. Further, in this research, the FPEF are considered specialized functions that use the primitive flow field variables to predict the appropriate flow physics within the domain.

Similar analysis were conducted by many authors<sup>4-5</sup>, resulting in varying degrees of shock identification and location. For example, a technique based on the theory of characteristics was introduced by Kanamori et al.<sup>7</sup> where they circumvent the problem of locating the region of steep spatial gradients with respect to the primitive variables. In another example, Lovely et al.<sup>5</sup> introduced a method that takes advantage of the fact that pressure gradients are always normal

to the shocks and the Mach number normal to the shock has at least a value of one before the shock. In a similar research study, Pagendarm et al.<sup>6</sup> proposed a method that locates shocks waves by searching the maxima of density gradient. However, only the method proposed by Pagendarm et al.<sup>6</sup> can capture expansion waves and compression waves, whereas the other two techniques capture compression waves only. Also, there are numerical difficulties associated with shock detection. Although shocks are sharp discontinuities on the primitive variable field, the shocks are smeared over several grid cells, due to errors in the numerical implementation<sup>8</sup>. Therefore, some shocks are undetected by the algorithm or the numerical oscillations may produce false indications. As a result, filtering is required so that weak shocks are detected and false indications are eliminated from the solution. Unfortunately, defining a threshold for the filtering function is not a trivial task and may vary from problem to problem. Ziniu et al.<sup>9</sup> proposed a new filtering criteria that takes into account the local mesh size and the absolute pressure. However, the filtering criteria also requires also a threshold and they suggested a value of  $\epsilon = 0.001$ . In practical applications, different FPEF may be required, depending on the local conditions and the properties of the flow, i.e: zone with considerable rotation, strain or significant changes in entropy. These different FPEF will complement the traditional way of using contour plots from the primitive variables.

Equation (10) shows the first FPEF based on the gradient of density in the direction of the velocity proposed by Pagendarm et al.<sup>6</sup>.

$$\frac{d\rho}{dn} = \nabla\rho \cdot \frac{\bar{V}}{|\bar{V}|} \quad (10)$$

Condition  $d\rho/dn > 0$  corresponds to compression waves and when  $d\rho/dn < 0$  corresponds to expansion waves. The mathematical formulation for a stationary shock wave based on the normal Mach number presented by Lovely et al.<sup>5</sup> is shown in equation (11).

$$Ma_n = \frac{Ma \cdot \nabla p}{|\nabla p|} = 1 \quad (11)$$

Although this study used equation (10) without filtering, the filtering criteria proposed by Ziniu et al.<sup>9</sup> with a threshold of  $\epsilon = 0.007$  is used to filter the solution from equation (11). Functions independent from steep gradients are beneficial, since they do not rely exclusively on sharp discontinuities on the primitive variables. Therefore, functions relating kinematics and thermodynamics are very useful and effective. Equation (12) shows Crocco<sup>10</sup> equations and the magnitude of the entropy gradient is represented in equation (13). Shocks waves are a truly inviscid phenomenon and therefore equation (12) can be used to locate shocks waves, since gradients in entropy give rise to rotation and equation (13) demonstrates that flow is rotational behind shocks. However, it is important to mention that equation (13) and (14) are only valid outside boundary layers.

$$\bar{V} \times (\nabla \times \bar{V}) = \nabla h_0 - T \nabla S \quad (12)$$

$$|\nabla S| = \sqrt{\left(\frac{u_j(\nabla \times \bar{V})}{T} - \frac{\partial h_0}{T \partial x}\right)^2 \hat{i} + \left(-\frac{u_i(\nabla \times \bar{V})}{T} - \frac{\partial h_0}{T \partial y}\right)^2 \hat{j}} \quad (13)$$

Another function based exclusively on fluid kinematics is the Q-criterion proposed by Hunt et al.<sup>11</sup>. They found that identifying regions in a flow field can provide important information that can describe and characterize important flow features. Equation (14) represents the Q-criterion and it represents the local balance between strain and vorticity, therefore it can determine zone with contractions and/or dilatation, proper of shock waves and zones where shear stresses is significant.

$$Q = \frac{1}{2} (\|\Omega\|^2 - \|S\|^2) \quad (14)$$

where  $\|\Omega\|$  and  $\|S\|$  represent the Euclidean norm of the vorticity and rate of strain tensor, respectively. Consequently, Q-criterion identifies vortices as areas with positive values, whereas negative values represent areas with high strain.

## THE IDS APPLICATIONS AND PHYSICS BASED EVALUATION

To demonstrate the physics capture capabilities of the IDS, two established fundamentals high Reynolds number fluid dynamic problems were numerically solved. The problems of interest in this study are as follows:

1. Hypersonic flow over a flat plate
2. The hypersonic flow cross jet interaction problem

Although similar problems were solved recently by Ferguson et al.<sup>4</sup> important improvements are presented in this study such as: Flow Feature Extractions Functions (FFEF) and cutting edge parallel libraries (MPI). These new features unmasked important flow characteristics that were not shown before in Ferguson et al.<sup>4</sup>; due merely to technical limitation.

### Hypersonic flow over a flat plate

Flow over a flat plate is the most general case of external and internal flows. Despite the simplicity of the boundary conditions and domain configuration, this problem remains as a classic fluid dynamic problem which is still used to validate and verify CFD schemes and codes<sup>12 13</sup>.

The role that Mach and Reynolds number play over the dynamic of the flow is important. Recent findings show that analytical approximations such as Van Driest II<sup>14</sup> is not accurately representing the velocity profile, especially under high heat flux<sup>15</sup>. Furthermore, the boundary layer thickness, temperature inside the boundary layer and coefficient of friction are strongly dependent to the Mach number. These effects are more pronounced in turbulent flows<sup>16</sup>. Therefore, it is important to demonstrate that IDS is capable of accurately reproducing these interactions to gain

insight on the structure of compressible boundary layers and understanding the influence of multiple fluid parameters on the flow dynamics.

This problem has inherent challenges. The instabilities change the flow type from laminar to turbulent. The inviscid-viscous interaction is quite complex and it is driven by the very large boundary layer thickness. In fact, the boundary layer height in hypersonic flows is proportional to  $M_\infty^2 / \sqrt{Re_x}$ <sup>16</sup>, and as a result, this interaction is stronger at high flow speed. The solution of the Navier-Stokes equations will be such that the computation could be divided into two different sections<sup>17</sup>. An outer section where inviscid laws dominate and can be solved using potential theory and an inner region where the viscous forces dominate and the Navier-Stokes equation must be used. The inconvenience of this approach is that the boundary layer height is required or it is an unknown variable in the process. To circumvent this issue, the full Navier-Stokes equations are used. However, the computational cost is very high, since the thinner portion of the boundary layer (viscous sub-layer) must be explicitly solved. In addition, an important limitation of the Navier-Stokes equations is the continuum of assumptions. The flow near the tip of the leading edge is described by kinetic theory, since free molecular flow exists<sup>18</sup>. However, the Navier-Stokes equations can describe with high accuracy the physics in this region<sup>18</sup>.

It is evident that this problem is interesting from the flow dynamic perspective. It encompasses all flow regimes in gas dynamics, from kinetic theory to continuum flow<sup>19</sup>. At supersonic conditions, a strong leading edge shock emanates from the leading-edge tip. This shock is also referred to as “*Bow Shock*”, due to its curvature; and the region between the surface and the shock wave is called “*Shock Layer*”<sup>13</sup>. In addition, the shock layer is divided in an inviscid region and viscous region. The latter, also known as “*Boundary Layer*”. The boundary layer undergoes important transition from laminar to turbulent and is also subdivided into two sub-regions. In the leading-edge region, the viscous-inviscid interactions are very strong and they affect the inviscid portion of the shock layer. In contrast, far from the leading edge, the viscous-inviscid interaction is weak. These two zones are known as strong interaction and weak interaction regions, respectively. These features impose computational constraints, in other words, the mesh must be fine enough to fully resolve the different regions while the computation remains stable, accurate and achieved in a timely manner.

Figure 1 provides a qualitative representation of the hypersonic flow over a flat plate problem whereas figure 2 represents a sketch of the computational domain. Consider the case of a hypersonic flow over the flat plate at a Mach number of 8.6, Reynolds number  $3.475771 \times 10^6$ , a Prandtl number of 0.70 and a specific heat ratio,  $\gamma$ , of 1.4. The freestream density, temperature, viscosity, and pressure were assumed to be  $2.2497 \times 10^{-2}$ , 360 K,  $2.117 \times 10^{-5}$  kg/ms and 2324.39 Pa, respectively. To obtain a grid independent solution a set of 5 different grid resolutions were proposed; ranging from 1001x1001 to 5001x16001 nodes in the streamwise and vertical direction respectively. The vertical direction dominated the grid generation since the gradients in the normal directions are the strongest in these types of configurations<sup>13</sup>.

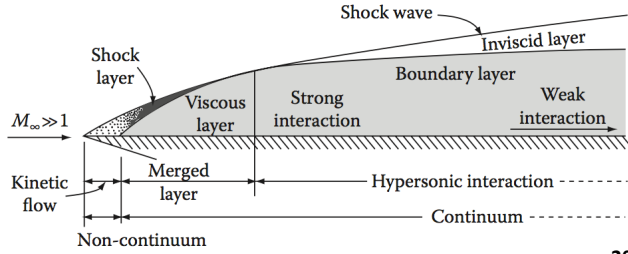


**Figure 1. Illustration of the flat plate problem<sup>20</sup>**

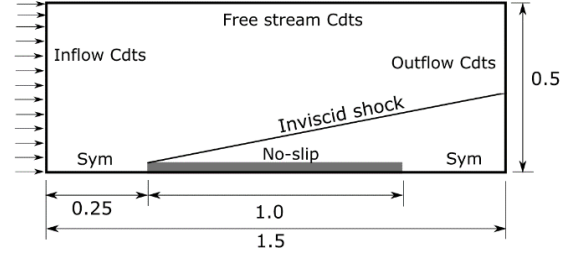


**Figure 2. Computational representation**

In this example, at the inflow and the far field boundaries, the primitive variables are assigned to their free stream values. At the exit plane, the flow primitive variables are extrapolated. As it is shown in figure 2, the bottom boundary is divided in three sections, representing the stationary wall (the flat plate), the leading and trailing edge gaps. Symmetric boundary condition is imposed to the leading and trailing edge gap. No-slip boundary condition and fixed wall temperature is assigned to the stationary wall, whereas density is extrapolated from the inner nodes. The temperature at the bottom wall is assigned at 1.0. The focus of this investigation is on the qualitative analysis of the IDS formulation and its capability to reproduce the physics associated with complex flowfields. The solution of the Navier-Stokes equations delivered by the IDS provides a set of four independent flowfield parameters, namely, density, velocity vector and temperature. Therefore, the grid independence studies were performed using these four primitive variables in two different locations; these are: one-half of the plate and at the outlet. In this report, only the plots corresponding to the half of the plates are shown (refer to figures 3-6). However, the trends found at the outlet agreed with the behavior from figures 3-6.

The plots illustrated in figures 3-6 show the vertical distribution of the primitive variables at 0.5 meters from the leading edge. The plots suggest a grid independent solution on the mesh 5001x16001 with a difference of 2.11% compared with the mesh 4001x8001. Another important feature from this study is the fact that figure 5 and 6 show a similar trend under the different meshes. Nevertheless, figures 3 and 4 depict important features that agree with other references and experimental data. Specifically, figure 4 shows the effect of viscous dissipation within the boundary layer<sup>16</sup>. The temperature starts increasing from the outer edge of the boundary layer towards the wall, reaching a peak somewhere between the outer edge and the wall. This trend is also found in Anderson<sup>21</sup> and Van Driest<sup>14</sup>. In turn, density decreases since pressure remains almost constant. Another important conclusion of this grid independence study is the fact that two important layers are observed from these plots; namely, the boundary layer and the shock layer. Figure 4 and 5 clearly depicted these two regions. It is inferred from these plots that the approximate height of the boundary layer is 0.01 non-dimensional height above the plate whereas the shock layer extends up to 0.08 non-dimensional units. Note that figures 3-6 indicate that the shock layer height predicted by the different meshes is approximate the same. Figures 3 and 4 confirm that the viscous effects properties of the boundary layer affect the magnitude of density and temperature, showing that the IDS scheme is consistent as the mesh size is reduced.

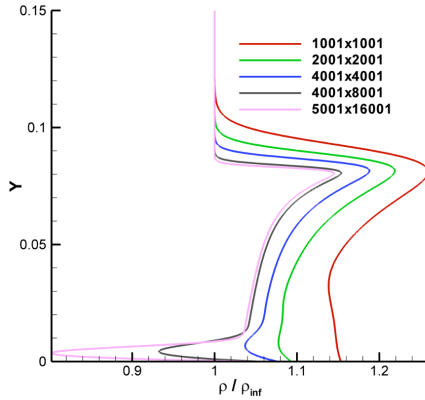


Figure 3. Density distribution at 0.5\*L

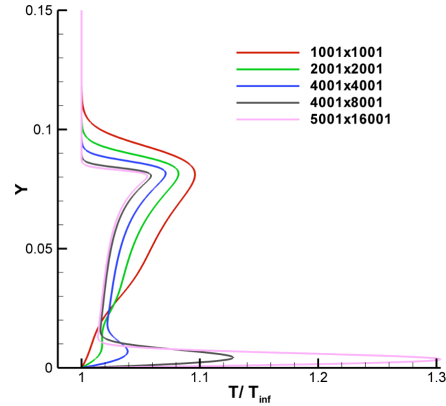


Figure 4. Temperature distribution at 0.5\*L

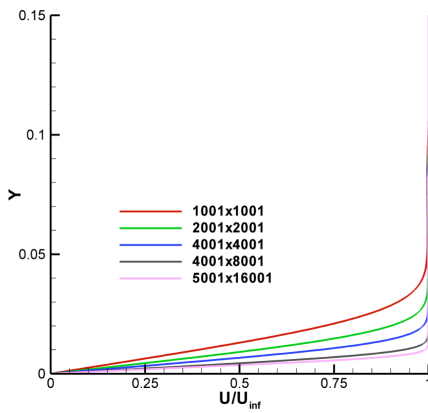


Figure 5. U-Velocity distribution at 0.5\*L

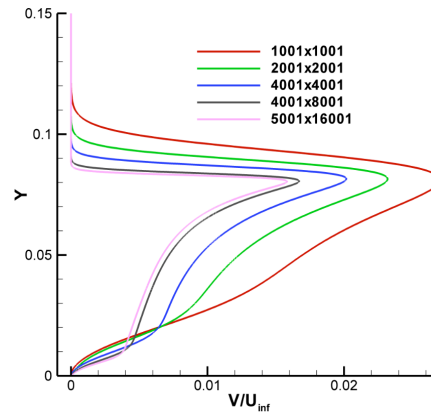


Figure 6. V-Velocity distribution at 0.5\*L

Contour plots of the four independent flowfield variables are shown in figures 7-10. These figures correspond to a small window from the complete data set. The objective of these contour plots is to show the region with strong interactions. For these types of problems, the zone nearest to the leading-edge tip is the regions with the strongest interactions and gradients.

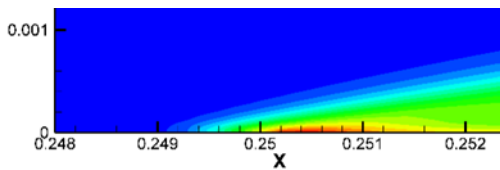


Figure 7. Density contour

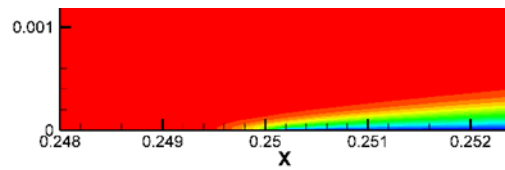


Figure 8. "U" Velocity contour

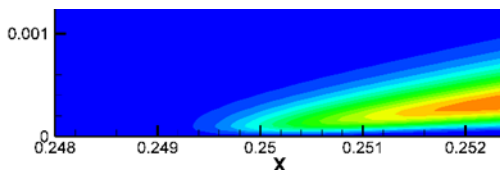


Figure 9. "V" Velocity contour

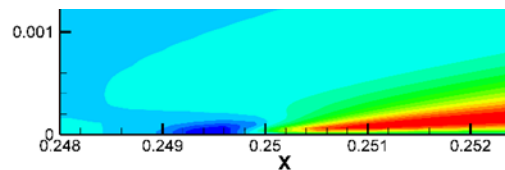
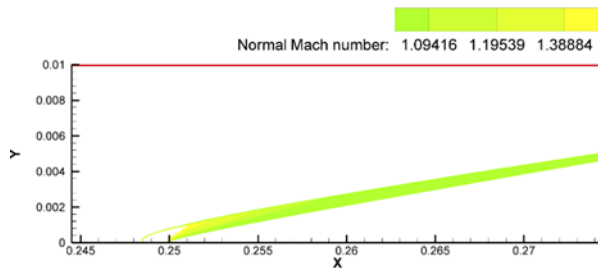


Figure 10. Temperature contour



Figures 7-10 show a region of the flat plate corresponding to  $0.248 \leq x \leq 0.253$  and  $0 \leq y \leq 0.00125$ . It is important to mention that these plots correspond to non-dimensional primitive variables. Figure 7 shows the density contour in the region represented by the window. It also shows a region with high density nearest to the leading edge corresponding to the jump in pressure, due to the shock emanating from the leading-edge tip. This jump in pressure results from the viscous interaction. On the other hand, figures 8 and 9 depict the growth of the boundary layer, whose thickness is smaller than the shock layer depicted in figure 7. The boundary layer and shock layer height is approximately 0.000528 and 0.001 units of non-dimensional units, at 0.252 units from the leading edge, respectively. Nonetheless, figure 9 demonstrated that the viscous interaction affects the inviscid region inside the shock layer. Figure 9 clearly shows that the inviscid lines are displaced upwards, even outside of the boundary layer. Quantitatively, figures 7-9 agree with figure 1. Also, figure 10 demonstrates that the highest temperature is concentrated in the region between the edge of the boundary layer and the wall, which was anticipated from figure 4 and has also been reported in prior research<sup>14</sup>. To elucidate important features, the flow feature extraction functions are analyzed and presented in figure 11-14.



**Figure 11. Normal Mach number contour**

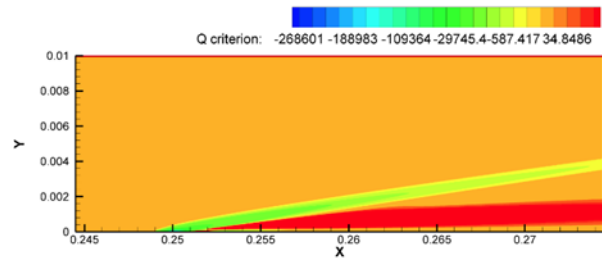


**Figure 12. Q- Criterion contour**

Figure 11 represents the Mach number normal to the shock, whose value is at least 1 just before the shock<sup>5</sup>. It can be observed that the bow shock starts slightly ahead of the tip and it has certain curvature. This characteristic was also reported in Mohling<sup>18</sup>. Also, figure 12 complements the information presented in the previous figures (figures 7-11). What is noteworthy, is the fact that figure 12 clearly shows three distinct layers; viscous layer, turbulent and inviscid layers. Figures 13 and 14 are the Q-criterion and vorticity plot at  $x = 0.27$ , respectively. They provide quantitative information that allows to characterize and describe these three layers. A viscous layer where Q-criterion is negative since the asymmetric tensor is negligible. This behavior is typical in viscous sub layers where the shear stress is laminar<sup>22</sup>. A second layer, named turbulent layer, where the swirling motions proper of turbulence flows make Q-criterion positive. In this region, viscosity contributes to create entropy and consequently vorticity<sup>23</sup>. Finally, an inviscid region where strain dominates over rotation and the flow is irreversible due to the presence of the shock that increases the pressure and temperature across the shock.

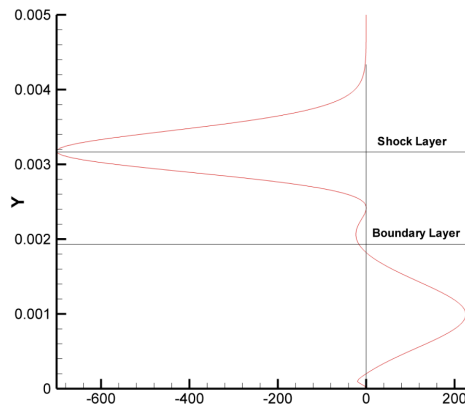


**Figure 13. Q-criterion (x=0.27)**

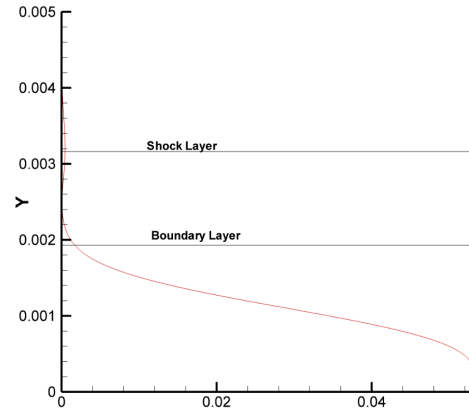


**Figure 14. Vorticity (x=0.27)**

Furthermore, it is important to note that the details of the: viscous, inviscid, merged and shock layer represented in figure 1, were accurately predicted by the IDS and demonstrated in figure 12. It can be concluded that both functions extract the shock-wave nearly on the same location. However, figure 11 shows a weak shock slightly ahead of the shock predicted by the Q-criterion.

### The hypersonic flow cross jet interaction problem

Consider a hypersonic flow over a flat plate where supersonic fuel is injected perpendicular to the freestream direction. The hypersonic current bends the supersonic flow injection yielding to complex interactions due to the presence of different shock waves and zones with recirculation and complex vortical structures. This flow configuration has important applications in the aerospace field, specifically in air-breathing hypersonic engines (Scramjets). Therefore, understating the flow behavior and the different complex structures is mandatory to increase the efficiency, decrease fuel consumption, flame stability and control the shock-wave boundary layer interactions. Due to short residence time, fuel mixing is an important parameter. In a previous research study, flow features of non-reacting and reacting were analysed including shock structures and interaction of vertical structures using Large Eddy Simulations (LES)<sup>24</sup>. They demonstrated that temperature and recirculation behind the flow injection created suitable conditions of auto-ignition and flame stability. Previously, Reynolds-Averaged Navier-Stokes equations (RANS) were used to investigate the details of the flow physics; findings demonstrated that the flow field was dominated by shock formations and their coupling with the strong vortical structures<sup>25</sup>. In addition, the pressure ratio of the jet to the freestream is the most important parameter. The penetration height and separation length was highly affected by the pressure ratio<sup>26</sup>. The latter group demonstrated that the boundary layer thickness played a minor role and that the slot width affects the flow field almost proportionally<sup>26, 27</sup>.

The present research does not consider chemical reactions and it focuses on predicting the complex interaction of different shock-wave structures and viscous – inviscid coupling using IDS. This study provides relevant details that can improve the understanding of the important features responsible for fuel mixing, combustion stability and pressure distribution. It is worth mentioning the challenges of this problem. Although we are solving the 2-D Navier Stokes

equations, there are essential features that are 3-D, such as: recirculation and vortex stretching. Nevertheless, we expect to predict those features accurately and extend this analysis under a 3-D framework. This study also considers that air is calorically perfect, although experimental data suggest that calorically imperfect gas should be used<sup>28</sup>.

Consider the case of hypersonic flow with a Mach number of 6.0 and a Reynolds number set to  $1.3047 \times 10^7$ , the Prandtl number set to 0.789 and the specific ratio set to 1.4. In addition, the freestream density, temperature, viscosity, and pressure were assumed to be  $0.090 \text{ kg/m}^3$ ,  $57.23 \text{ K}$ ,  $3.7655 \times 10^{-6} \text{ kg/ms}$ , and  $1478.26 \text{ Pa}$ , respectively. Figure 15 shows a representation of the flow field and figure 16 depicts the computational representation of the problem of interest along with the boundary conditions. Dimensions shown in figure 16 are in meters. As figure 15 shows, different features are depicted. Inviscid shock such as: Barrel, reattachment, bow and separation are present. Also, there are also two main recirculation zones located behind and ahead of the injection point. It is of interest to note that the recirculation zone is confirmed by a family of different coherent vortices that improve the mixing of air with fuel<sup>29</sup>.

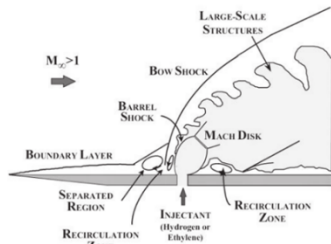


**Figure 15. Schematic view of structures<sup>30</sup>**

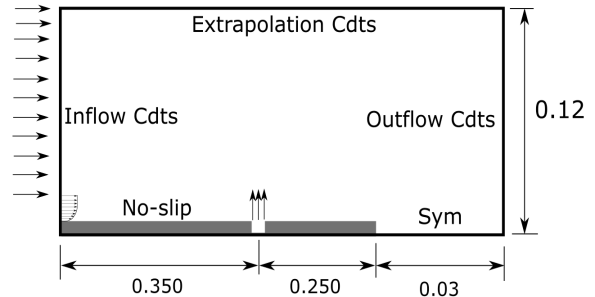


**Figure 16. Computational representation**

The 2-D computational domain was developed for a flat plate with a length of 0.6 and the height of the computational domain was 0.12 meters respectively. The lower plane, i.e: the bottom wall, corresponds to the solid surface of the flat plate. Vertical gradient for temperature and density were set to zero ( $\partial T / \partial y = \partial \rho / \partial y = 0.0$ ) and no-slip conditions were imposed on the flat plate. The jet was assumed to have a step profile, i.e: no boundary layer in the injection point was considered. The injector was simulated by a small gap of width  $1.644 \times 10^{-3}$  meters at the bottom wall at 0.350 meters from the leading edge. The Mach number of the injector was set to 1. The injection temperature and density was set to 4.5 a 21.0, respectively. Under these conditions, the pressure ratio between the injection point and the freestream is defined as 94.49. Extrapolation boundary conditions were used on the top boundary and at the exit plane (outlet). Finally, symmetric boundary conditions were used behind the flat plate. The boundary condition at the inlet was divided into two portions; one above and the other below the boundary layer height. The primitive variables were set to its freestream values for both portions, except for the horizontal component of the velocity vector. Although the flow upstream the injector is expected to be fully developed, and therefore turbulent, it was decided to use a laminar profile to define the velocity profile. This assumption combined with the length ahead of the injection point (0.350 meters) allows the boundary layer to develop to its proper equilibrium state. To define the

profile, an imaginary buffer length of 0.24 meters was used to compute the theoretical profile based on the Reynolds and Mach number used in this problem.

The 2-D solution provided by the IDS is a set of four independent flow field variables that describe the physics associated with the problem of interest. The grid sensitivity analysis is based on these four primitive variables and it followed the same methodology presented in the previous problem. Four set of grid solution were tested, ranging from 1001x1001 to 8001x8001 node points in the horizontal and vertical direction. The maximum difference between two consecutive grid refinements was 18 %. The boundary layer height at 0.163 non-dimensional units from the leading edge is approximately  $3.92 \times 10^{-3}$  meter height, whereas the height described by the expression used at the inlet boundary conditions was  $8.75 \times 10^{-5}$ . It was corroborated that the boundary developed up to its proper equilibrium.

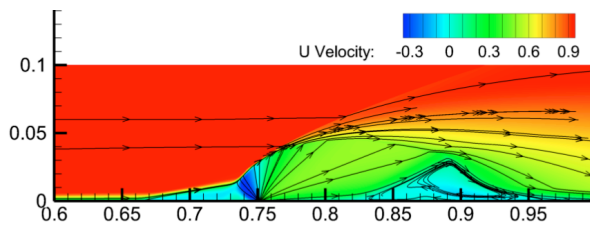


Figure 17. "U" velocity contour

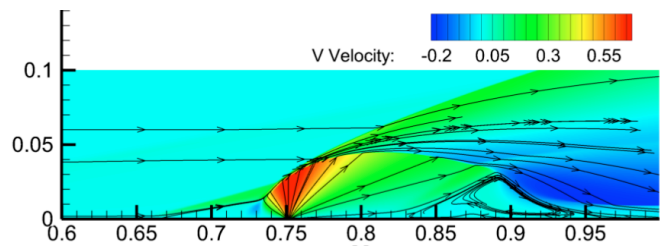
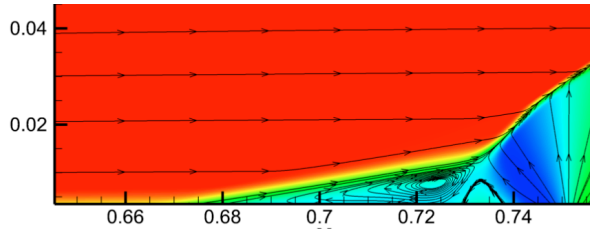


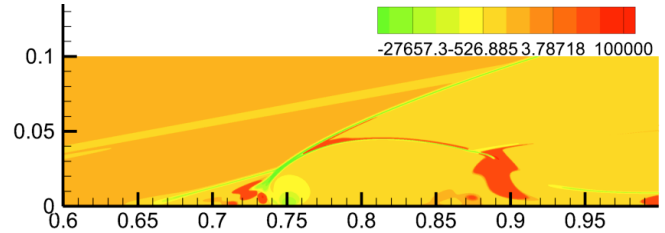
Figure 18. "V" velocity contour

Figures 17 and 18 show the horizontal and vertical components of the velocity vector. It can be inferred from these two plots that flow injection acts as an obstruction to the main stream flow, causing a bow shock. The stream-tracers corroborate this hypothesis merging ahead of the injection point. It is important to mention that to the author's knowledge there is no other published research that has produced findings similar to those that use the conditions utilized in this study, specifically when it comes to Re and Mach numbers. Nevertheless, common features are depicted in these two plots. Figures 17 and 18 clearly show two important separation zones (recirculation).

The strongest recirculation appears behind the injection section. Another small separation, ahead of the injection, is also reported in previous research Rana et al. <sup>31</sup> and in this case, this zone presents two vortices; one elongated that forms at the root of the separation region and another located closest to the low pressure zone where the injection point is located (fig. 19).



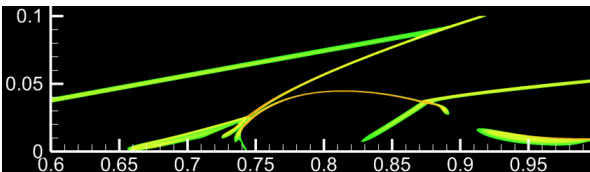
**Figure 19. "U" velocity contour**



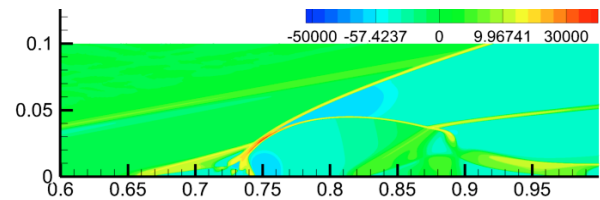
**Figure 20. Q- Criterion**

Figure 20 represents the Q-criterion and it corroborates that there are mainly two recirculation zones, colored in light red.

Also, figure 20 demonstrates that the features shown as steep gradients on both components of the velocity vector correspond to zones with intense strain, highly negative values of Q-criterion, colored by light green. Figures 21 and 22 represent the Normal Mach number and the Normal density gradient plots, respectively. Both figures agree on the prediction of the compression waves and they show the complete shock structures, namely: bow, separation, barrel, reattachment shocks and expansion waves. Furthermore, it is evident that figure 22 complements figure 21 since it provides evidence about expansion zones, colored in light green and blue zones (negative values). It is of interest to note the disadvantage of relying only on the primitive variables. Although figures 17 and 18 agree with the bow shock predicted by figures 21 and 22, it is not possible to identify the reattachment and barrel shock shown in figures 21 and 22.



**Figure 21. Normal Mach number plot**



**Figure 22. Normal Density gradient**

Figures 23 and 24 provide evidence of the dynamic of the flow in the injection section. As the jet emerges into the main stream, the supersonic flow expands as it is shown in figure 23 with the vectors representing the expansion fans. It is seen that the barrel shock obtained in this case is wider compared to the Rana et al.<sup>11, 31</sup>, these discrepancies are due to the difference in Mach and Reynolds Number. As the supersonic flow meets the subsonic region behind the bow shock, another shock forms called "Barrel Shock". This shock is clearly shown by Figures 21 and 22, also, figure 24 provides evidence of this zone since pressure drastically changes through this area.

One important difference is the size of the recirculation zone that forms behind the injection point and the compression shocks that emanates at the reattachment point. In contrast to previous research studies such as: Viti et al.<sup>25</sup>, Rana et al.<sup>31</sup> and Kawai et al.<sup>32</sup> the injection plume is pushed along the main flow, decreasing penetration of the cross-flow. Also, the region behind the injection is attached to the bottom wall, whereas the previous studies show a separation bubble. It is important to mention that difference in the momentum ratio used in this research study (Mach =6.0) causes the difference in the location of the separation bubble.

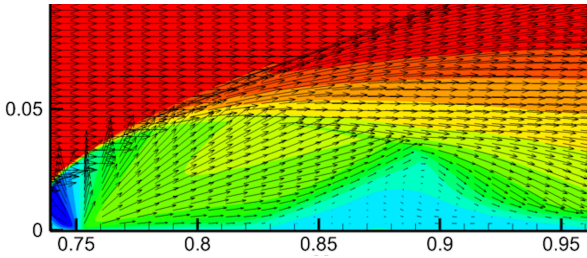


**Figure 23. “U” velocity component with vector**

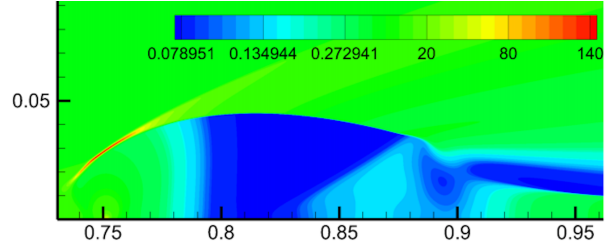


**Figure 24. Pressure Contour**

The figure 23 shows that the flow is attached up to approximately 0.83 non-dimensional units where the flow separates and form the bubble shown in figure 23. The low-pressure zone produced by the expansion fans cause a local acceleration of the fluids causing a secondary separation waves and subsequently expansions waves that produces a secondary local acceleration that end up with the final reattachment shock wave. It is noteworthy to mention the complex pressure field of this problem caused by low pressure due to the expansion fans at the injection point and the high-pressure level caused by the bow shock. The combination of these two phenomena cause the secondary separation bubble that strongly affects the flow downstream.

## CONCLUSIONS

A new numerical scheme for solving the 2D Navier Stokes equations was validated using Flow Feature extraction functions to demonstrate the physics based capabilities of the new scheme called IDS. At this stage of development, it was demonstrated that the IDS has the capabilities to predict the complex structure of the problem solved in this research study. This scheme is called the Integro-Differential Scheme (IDS) and it uses a method of consistent averages to provide an explicit scheme time marching solution. It was demonstrated that different FFEF are required to extract important information directly and accurately. A set of functions are required since one function by itself cannot reveal all the details due to their sensibility to numerical dissipation. Therefore, these functions complement the traditional approach of using contour plots of primitive variables to locate shocks waves.

## ACKNOWLEDGEMENTS

The authors would like to acknowledge Professor Kenneth M Flurchick from the Department of physics and Computational Science and Engineering program at North Carolina Agricultural and Technical State University (NCAT) for his guidance and advice on developing the parallel version of IDS. The computational resources used in this research were made available in part by a grant from the National Science Foundation Grant no.#1429464, entitled MRI: Acquisition of CRAY XC-30 HPC Cluster to Support NCAT Research Computing, Education and Outreach. Also, the first author would like to thank Maida Bermudez Bosch for her help on editing and proofreading the written research article.

## CONTACT AUTHOR EMAIL ADDRESS

The corresponding author can be contacted by email at the following address:  
fferguso@ncat.edu

## REFERENCES

1. F. Ferguson and G. Elamin, Advanced Computational Methods in Heat Transfer IX, 97 (2006).
2. M. Griebel, T. Dornseifer and T. Neunhoeffler, *Numerical simulation in fluid dynamics: a practical introduction*. (SIAM, 1998).
3. F. Ferguson, M. Dhanasar and N. Dasque, presented at the 49th AIAA Aerospace Sciences Meeting including the New Horizons Forum and Aerospace Exposition, 2011 (unpublished).
4. F. Ferguson, H. Mrema and M. Dhanasar, presented at the 53rd AIAA Aerospace Sciences Meeting, 2015 (unpublished).
5. D. Lovely and R. Haimes, AIAA paper **3285**, 1999 (1999).
6. H.-G. Pagendarm, B. Seitz and S. Choudhry, in *Shock Waves@ Marseille I* (Springer, 1995), pp. 353-358.
7. M. Kanamori and K. Suzuki, Journal of Computational Physics **230** (8), 3085-3092 (2011).
8. K.-L. Ma, J. Van Rosendale and W. Vermeer, presented at the Proceedings of the 1996 symposium on Volume visualization, 1996 (unpublished).
9. Z. Wu, Y. Xu, W. Wang and R. Hu, Chinese Journal of Aeronautics **26** (3), 501-513 (2013).
10. L. Crocco, ZAMM-Journal of Applied Mathematics and Mechanics/Zeitschrift für Angewandte Mathematik und Mechanik **17** (1), 1-7 (1937).
11. J. C. Hunt, A. A. Wray and P. Moin, (1988).
12. M. Holden and T. Wadhams, AIAA paper **1137**, 2003 (2003).
13. D. John and J. Anderson, P. Perback, International ed., Published (1995).
14. E. R. Van Driest, Journal of the Aeronautical Sciences (2012).
15. D. Modesti and S. Pirozzoli, International Journal of Heat and Fluid Flow **59**, 33-49 (2016).
16. J. D. Anderson, *Hypersonic and high temperature gas dynamics*. (Aiaa, 2000).
17. H. Schlichting and K. Gersten, *Boundary-layer theory*. (Springer Science & Business Media, 2003).
18. R. A. Mohling, (1972).
19. W. Chow, AIAA Journal **5** (9), 1549-1557 (1967).
20. R. H. Pletcher, J. C. Tannehill and D. Anderson, *Computational fluid mechanics and heat transfer*. (CRC Press, 2012).
21. J. D. Anderson, *Modern compressible flow: with historical perspective*. (McGraw Hill Higher Education, 2003).
22. P. Davidson, *Turbulence: an introduction for scientists and engineers*. (Oxford University Press, USA, 2015).
23. H. Babinsky and J. K. Harvey, *Shock wave-boundary-layer interactions*. (Cambridge University Press, 2011).

24. S. H. Kim, P. Donde, V. Raman, K.-C. Lin and C. Carter, presented at the 50th AIAA Aerospace Sciences Meeting Including the New Horizons Forum and Aerospace Exposition, 2012 (unpublished).
25. V. Viti, R. Neel and J. A. Schetz, *Physics of Fluids* **21** (4), 046101 (2009).
26. R. Amano and D. Sun, presented at the The 24th Congress of ICAS, 2004 (unpublished).
27. D. P. Rizzetta, *AIAA journal* **30** (10), 2434-2439 (1992).
28. R. Pecnik, V. Terrapon, F. Ham and G. Iaccarino, *Annual Research Briefs*, 33-45 (2009).
29. K. Mahesh, *Annual Review of Fluid Mechanics* **45**, 379-407 (2013).
30. M. Gruber, A. Nejad, T. Chen and J. Dutton, *Journal of Propulsion and Power* **11** (2), 315-323 (1995).
31. Z. A. Rana, D. Drikakis and B. J. Thornber, presented at the Proceedings of 27th Congress of the International Council of the Aeronautical Sciences (ICAS-2010), Nice, France.(ISBN: 9780956533302), 2010 (unpublished).
32. S. Kawai and S. K. Lele, *AIAA journal* **48** (9), 2063-2083 (2010).